JGR Solid Earth

RESEARCH ARTICLE
10.1029/2022JB024962

Archaeomagnetism in the Levant and Mesopotamia Reveals the Largest Changes in the Geomagnetic Field

Ron Shaar[1], Yves Gallet[2], Yoav Vaknin[1,3], Lilach Gonen[1], Mario A. S. Martin[3], Matthew J. Adams[4], and Israel Finkelstein[3,5]

[1]The Institute of Earth Sciences, The Hebrew University of Jerusalem, Jerusalem, Israel, [2]Université Paris Cité, Institut de Physique du Globe de Paris, CNRS, Paris, France, [3]Institute of Archaeology of Tel Aviv University, Tel Aviv, Israel, [4]W.F. Albright Institute of Archaeological Research, Jerusalem, Israel, [5]School of Archaeology and Maritime Cultures, University of Haifa, Haifa, Israel

Abstract Our understanding of geomagnetic field intensity prior to the era of direct instrumental measurements relies on paleointensity analysis of rocks and archaeological materials that serve as magnetic recorders. Only in rare cases are absolute paleointensity data sets continuous over millennial timescales, in sub-centennial resolution, and directly dated using radiocarbon. As a result, fundamental properties of the geomagnetic field, such as its maximum intensity and rate of change have remained a subject of lively discussion. Here, we place firm constraints on these two quantities using Bayesian modeling of well-dated archaeomagnetic intensity data from the Levant and Upper Mesopotamia. We report new data from 23 groups of pottery collected from 18 consecutive radiocarbon-dated archaeological strata from Tel Megiddo, Israel. In the Near East, the period of 1700–550 BCE is represented by 84 groups of archaeological artifacts, 55 of which were dated using radiocarbon or a direct link to clear historically dated events, providing unprecedented sub-century resolution. Moreover, stratigraphic relationships between samples collected from multi-layered sites enable further refinement of the data ages. The Bayesian curve shows four geomagnetic spikes between 1050 and 600 BCE, with virtual axial dipole moment (VADM) reaching values of 155–162 ZAm^2, much higher than any prediction from geomagnetic field models. Rates of change associated with the four spikes are ~0.35–0.55 μT/year (~0.7–1.1 ZAm^2/year), at least twice the maximum rate inferred from direct observations spanning the past 180 years. The increase from 1750 to 1030 BCE (73–161 ZAm^2) depicts the Holocene's largest change in field intensity.

Plain Language Summary The strength of Earth's magnetic field changes in an unpredictable manner. Understanding these changes requires precise information on how the field has changed in the past. Direct instrumental measurements of magnetic field intensity began in the 1840s, providing only a short time window into past intensity changes. Here, we explore the ancient field by analyzing a rare collection of radiocarbon-dated archaeological materials from stratified archaeological settlements and historically dated burnt structures in the Levant and Mesopotamia. We use new data from Tel Megiddo (Armageddon) to construct a continuous curve of geomagnetic field intensity spanning 2,500 years, with unprecedented detail and resolution. The curve depicts the evolution of a high-intensity anomaly, the largest change in intensity observed during the Holocene. Between 1750 and 1050 BCE, the field rapidly increased to values greater than twice those of today, much higher than any prediction derived from available geomagnetic field models. Subsequent oscillations between 1050 and 550 BCE, with extreme peaks, namely "geomagnetic spikes," reveal change rates of at least twice as fast as the fastest change observed since the advent of direct measurements. Levantine archaeomagnetic data represent a case study in which archaeology provides crucial constraints on the geomagnetic field behavior.

Key Points:

- Archaeomagnetic intensity data from 23 groups of pottery collected from 18 consecutive radiocarbon-dated strata in Tel Megiddo (Israel)
- The Levantine Archaeomagnetic Curve (LAC): a Bayesian radiocarbon-calibrated archaeointensity curve of the Levant and Mesopotamia
- Four geomagnetic spikes between 1050 and 600 BCE define new constraints for maximum field intensity and secular variation rates

Supporting Information:

Supporting Information may be found in the online version of this article.

Correspondence to:

R. Shaar,
ron.shaar@mail.huji.ac.il

Citation:

Shaar, R., Gallet, Y., Vaknin, Y., Gonen, L., Martin, M. A. S., Adams, M. J., & Finkelstein, I. (2022). Archaeomagnetism in the Levant and Mesopotamia reveals the largest changes in the geomagnetic field. *Journal of Geophysical Research: Solid Earth*, *127*, e2022JB024962. https://doi.org/10.1029/2022JB024962

Received 11 JUN 2022
Accepted 4 DEC 2022

Author Contributions:

Conceptualization: Ron Shaar, Yves Gallet, Israel Finkelstein
Formal analysis: Ron Shaar, Yves Gallet, Yoav Vaknin, Lilach Gonen
Funding acquisition: Ron Shaar, Yves Gallet, Israel Finkelstein
Investigation: Ron Shaar, Yves Gallet, Mario A. S. Martin, Israel Finkelstein
Methodology: Ron Shaar, Yves Gallet, Yoav Vaknin, Israel Finkelstein

1. Introduction

The absolute intensity of the geomagnetic field was first measured by Carl Friedrich Gauss in 1832 (Courtillot & Le Mouel, 2007). Subsequent measurements with improved precision and spatial resolution have provided quantitative estimates of the amplitude and rate of geomagnetic field intensity changes, but only across the past two centuries. Information from periods preceding observational measurements, fundamental for understanding the magnetic field behavior, is derived from ancient materials that acquired thermoremanent magnetization upon cooling from high temperatures. For the past several millennia, archaeological materials have been

Project Administration: Ron Shaar, Israel Finkelstein
Resources: Ron Shaar, Mario A. S. Martin, Matthew J. Adams, Israel Finkelstein
Supervision: Ron Shaar
Validation: Ron Shaar, Yves Gallet
Visualization: Ron Shaar
Writing – original draft: Ron Shaar, Yves Gallet, Yoav Vaknin, Israel Finkelstein
Writing – review & editing: Ron Shaar, Yves Gallet, Yoav Vaknin, Matthew J. Adams, Israel Finkelstein

the primary source for this information (Arneitz et al., 2017; Brown et al., 2021), providing most of the data for late Holocene geomagnetic models (Arneitz et al., 2019; Campuzano et al., 2019; Constable et al., 2016; Nilsson et al., 2014, 2022; Panovska et al., 2019; Pavon-Carrasco et al., 2014). However, global models are smoothed by design, as they require a tradeoff between model complexity and fit to heterogeneous data. Regional intensity curves provide important insights into field behavior (Cai et al., 2017; Garcia et al., 2021; Genevey et al., 2016, 2021; Rivero-Montero et al., 2021; Schnepp et al., 2020), but they depend on the quality of the underlying source data. One of the most significant limiting factors for both global and regional field modeling is the precision and accuracy of the published ages. Only ∼12% of the global published data from the past 10 kyr data are directly dated with radiocarbon, and in many cases, the exact nature and context of the dated material are not documented. Instead, most archaeomagnetic ages are based on assignment to regional archaeological chronologies, which may have differing interpretations, can be poorly tied to absolute ages, or have large age ranges (Shaar et al., 2020). Furthermore, unlike paleomagnetic field direction reconstructions, which use stratigraphic constraints in sedimentary sequences to obtain continuous time series, archaeomagnetic intensity (archaeointensity) data sets are mostly sporadic in time and space. Given the overall uncertainties in the available paleomagnetic and archaeomagnetic data, some of the most fundamental properties of the geomagnetic field, such as its maximum intensity and maximum possible rate of change, have remained elusive and the subject of a lively and fruitful debate (Davies & Constable, 2018; Korte & Constable, 2018; Livermore et al., 2014, 2021).

One way to improve the resolution of archaeomagnetic data is to focus efforts on large multi-layered archaeological sites, which are composed of distinct consecutive strata, and can provide data in stratigraphic order, for example, Mari (Tell Hariri), Tell Atij and Tell Gudeda in Upper Mesopotamia (Gallet & Butterlin, 2015; Gallet et al., 2006, 2008, 2020), Ebla (Tell Mardikh) in Northern Levant (Gallet et al., 2008, 2014), and Tel Hazor in Southern Levant (Shaar et al., 2016, 2020). Although these are key sites for Near Eastern archaeology, most of their archaeomagnetic data are not radiocarbon-dated. From this perspective, Tel Megiddo (Israel), with a radiocarbon-based age model covering timespan of 3000–735 BCE, is unique, providing an unprecedented opportunity to construct a stratigraphically constrained radiocarbon-calibrated archaeomagnetic time series.

In the following, we report data obtained from Tel Megiddo, which to date, is the largest archaeointensity data set available from a single site. We compile the new data with other archaeomagnetic data from the Levant and Mesopotamia that pass our selection criteria. The temporal resolution of the combined data between the eighteenth and the sixth century BCE is a century or less, as most of the archaeomagnetic ages in this period are derived from radiocarbon-dated contexts and historically dated burnt structures. Using this high-precision compilation, we develop the Levantine Archaeomagnetic Curve (LAC), utilizing a Bayesian methodology. The LAC elucidates the details of the largest geomagnetic change in the Holocene, associated with the Levantine Iron Age Anomaly (Shaar et al., 2016) and the occurrence of geomagnetic spikes (Ben-Yosef et al., 2009; Shaar et al., 2011, 2016). We use the LAC to enhance knowledge of the number, duration, and intensity of geomagnetic spikes, which define new robust upper limit constraints for both maximum field intensity and rate of change.

2. Archaeomagnetic Intensity Stratigraphy of Tel Megiddo

2.1. Background

Tel Megiddo (32.585°N, 35.185°E, Figure 1) is a world-heritage archaeological site located on the western margins of the Jezreel Valley in northern Israel. Owing to its strategic location on the international route which connected Egypt with Mesopotamia, Megiddo was a central city and an important administrative center throughout the Bronze and Iron Ages (ca. 3500–600 BCE). Extensive excavations of the mound have revealed more than 30 Bronze and Iron Age superimposed settlements, with several destruction layers indicating violent endings in military campaigns (Finkelstein, 2009). The chronology of the entire Megiddo sequence was established from Bayesian analyses of ca. 150 radiocarbon samples (the total number of radiocarbon samples at Megiddo is 185) carefully collected from nearly all strata (Boaretto, 2022; Martin et al., 2020; Regev et al., 2014; Toffolo et al., 2014). Special care was taken in assembling the radiocarbon model from mostly short-lived organic materials strongly linked to the archaeological findings. The exceptionally large radiocarbon data from a detailed, continuous, and well-established stratigraphy, along with the intensive ceramic record of Megiddo that defines the relative dating of the region (e.g., late Iron I, early Iron IIA), provide a robust absolute chronology for Near Eastern archaeology.

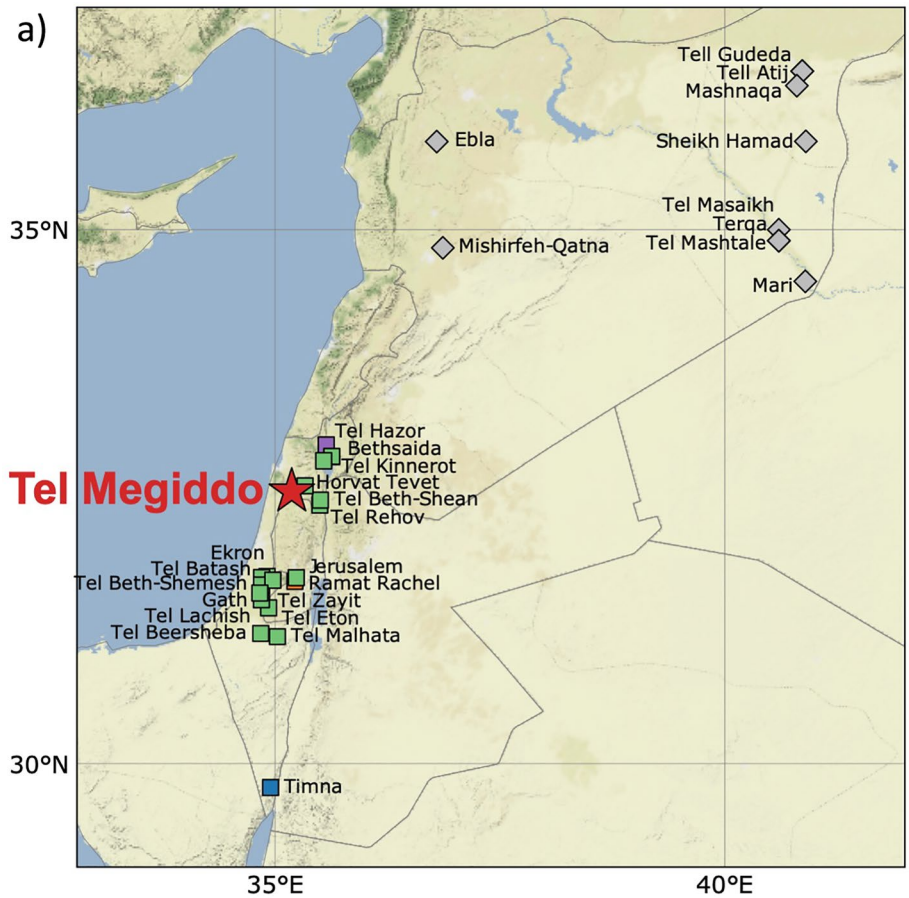

Figure 1. Map showing Tel Megiddo and other sites in the Levant and Western Upper Mesopotamia used to construct the Levantine Archaeomagnetic Curve (LAC.v.1.0) shown in Figure 6. Color code is as in Figure 6.

The archaeomagnetic stratigraphy of Tel Megiddo is based on 23 different contexts recovered from 18 layers, excavated in six excavation areas (Figure 2). Ten contexts (S-3, H-15, K-6, H-11, K-4/H-9/Q-7, Q-4, and H-3/Q-2) are destruction layers with distinct boundaries and clear marks of their ending. Megiddo's final destruction by the Assyrian Tiglath-Pileser III is conclusively dated to 732 BCE, based on multiple historical documents. We sampled fragments of indicative pottery from each context, with emphasis on local domestic material. We preferred, when possible, complete or cured vessels that were photographed and documented in the excavation reports. In three contexts (Q-4, Q-5, and K-9), we also sampled fragments of cooking ovens (tabuns). The fragments (termed hereafter "samples"for consistency with previous publications) discussed here include new data, as well as data already published in Shaar et al. (2016) and Shaar et al. (2020), which reported the initial archaeomagnetic stratigraphy of Megiddo. Table S1 lists the archaeological details of all the materials analyzed in this study.

2.2. Archaeointensity Experiments

Thellier-IZZI-MagIC paleointensity experiments were conducted in the shielded paleomagnetic laboratory at the Institute of Earth Sciences, the Hebrew University of Jerusalem, using two modified ASC TD-48 ovens and a 2G-RAPID superconducting rock magnetometer. Specimens were prepared by gluing small pieces of pottery inside non-magnetic $22 \times 22 \times 20$ mm square alumina crucibles. The protocol followed the IZZI method (Tauxe & Staudigel, 2004; Yu et al., 2004) with routine pTRM checks at every second temperature step using an oven field of 40, 50, or 60 μT. Heating time ranged from 40 to 65 min, depending on the target temperature. In total, each IZZI experiment included 31 or 33 heating steps at 13 or 14 temperature intervals between 100°C and 590°C or 600°C. All specimens were subjected to anisotropy of thermoremanent magnetization

a)

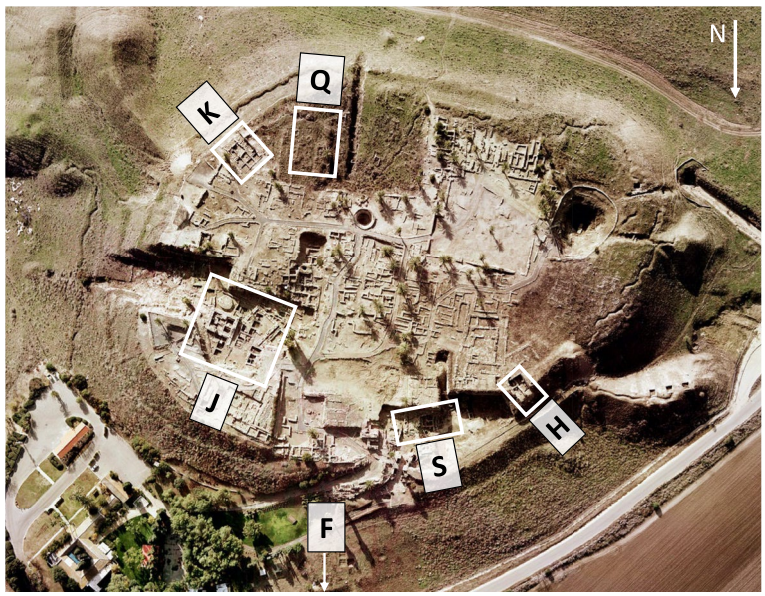

b)

Period \ Area	J	S	F	K	H	Q
Early Iron IIB					H-3	Q-2
Late Iron IIA						Q-4
Middle Iron IIA					H-7	Q-5
Early Iron IIA						Q-6
Late Iron I				K-4	H-9	Q-7
Middle Iron I					H-10	
Early Iron I					H-11	
Late Bronze III				K-6		
Late Bronze IIB				K-8		
Late Bronze IIA-IIB				K-9		
Late Bronze I			F-10		H-15	
Middle Bronze III				K-10		
Middle Bronze III				K-11		
Middle Bronze II			F-13			
Middle Bronze I		S-3				
Early Bronze III	J-6					
Early Bronze III	J-5					
Early Bronze IB	J-4					

Figure 2. Tel Megiddo. (a) Aerial photo of the mound displaying the excavation areas discussed in the text. (b) Tel Megiddo stratigraphy showing all the contexts analyzed for archaeointensity. The shaded cells mark destruction layers.

(ATRM) experiments, which consisted of eight heating steps at 590°C or 600°C: a baseline zero-field step, six infield steps at orthogonal directions, and an additional alteration check. ATRM alteration parameter was calculated following Shaar et al. (2015) (Table 1). For specimens with ATRM alteration checks >6%, anisotropy of anhysteretic remanent magnetization (AARM) was measured at six orthogonal directions, after thermal demagnetization of the specimens, using 100 mT AC field and 0.10 mT DC bias field. All specimens were subjected to cooling rate correction experiments, which consisted of cooling from either 590°C or 600°C to room temperature in 4–5 steps, following the protocol described in Shaar et al. (2020). Archaeointensity values were calculated with the *Thellier-GUI* program (Shaar & Tauxe, 2013), incorporated into the *PmagPy* software package (Tauxe et al., 2016), using *Thellier Auto Interpreter* algorithm and the acceptance criteria listed in Table 1. Sample results were calculated by averaging at least 3 specimens per sample using the STDEV-OPT algorithm of the *Thellier-GUI* program and the "extended error bounds" approach (Shaar & Tauxe, 2013; Shaar et al., 2016). When averaging sample data in "groups" (see Section 2.3), we calculated an arithmetic mean of the STDEV-OPT values of the samples. A detailed description of the methods can be found in Shaar et al. (2016) and Shaar et al. (2020). All measurement data are available in the MagIC database (https://www.earthref.org/MagIC/19395).

2.3. Results

The archaeomagnetic data from Tel Megiddo, including the data already published in Shaar et al. (2016) and Shaar et al. (2020), include 763 specimens from 175 samples. In this study, we analyze 288 specimens from 85 newly collected samples. In total, 583 specimens and 132 samples pass the criteria listed in Table 1, where archaeointensities obtained at the sample level are calculated from a minimum of 3 specimens. Figure 3 shows representative cases of a successful specimen and interpretations failing criteria. The importance of the anisotropy and cooling rate corrections is illustrated in Figure 4. Typically, the bias due to anisotropy and cooling rate effects is 5%–15%; in some cases, the combined corrections exceed 20%. Table S2 lists specimens results, anisotropy and cooling rate correction factors, and values of paleointensity statistics listed in Table 1.

Figure 5 displays sample data with error bars calculated using the "extended error bounds" approach (Shaar & Tauxe, 2013). In general, samples collected from the same archaeological context (termed hereafter "group") show good agreement with only two outliers in groups K-4 and Q-4. Levels H-9 and H-3 exhibit a large dispersion

Table 1
Acceptance Criteria, LAC.v.1.0

Criteria group [a]	Statistic	Threshold value	Description	Reference[a]
Specimen	FRAC	0.79	Fraction parameter	Shaar and Tauxe (2013)
	β	0.1	Scatter parameter	Coe et al. (1978); Selkin and Tauxe (2000)
	SCAT	True	Scatter parameter	Shaar and Tauxe (2013)
	GAP-MAX	0.5	Maximum gap	Shaar and Tauxe (2013)
	N_{PTRM}	2	Number of pTRM checks	
	N	5	Number of data points	
	MAD	5	Maximum Angular Deviation of the zero field steps	Kirschvink (1980)
	DANG	10	Deviation Angle	Tauxe and Staudigel (2004)
	Alteration check (correction)	6%	Alteration check in TRM anisotropy and cooling rate experiments	Shaar et al. (2015)
Sample (pottery vessel, furnace, brick, slag)	N_{min}	3	Number of specimens	
	$N_{min\_aniso\_corr}$	At least half of the specimens	Minimum number of specimens with anisotropy correction	
	$N_{min\_cr\_corr}$	1	Minimum number of specimens with cooling rate correction	
	σ	$\sigma < 3$ μT or $\sigma < 8\%$	Standard deviation of the sample mean	
	Anisotropy sample test	6%	If the mean anisotropy correction of all the specimens from the same sample (fragment) is higher than this value, specimens without anisotropy correction are discarded	

[a]For a complete description and definitions of paleointensity statistics, see Paterson et al. (2014).

of data, with distinctively different values. As the ceramics in each context represent production during a time interval rather than a singular point in time, this probably indicates fast changes in the field during the interval represented in the ceramic assemblage. Thus, we tentatively split the results from these two contexts into two subgroups. The mean archaeointensity of each group is calculated by averaging the sample means. Detailed sample data are provided in Table 2 and Table S3. The archaeomagnetic stratigraphy presented in Figure 5 (Table 2) shows exceptionally large amplitude changes: between ∼39 and ∼90 μT.

The ages of the groups are based on the Bayesian age model of Megiddo, which is assembled from ∼150 radiocarbon samples and takes into account the stratigraphic relationships between strata and correlation between levels excavated at different areas (e.g., Figure 2). The published 68.2% and 95.4% probability age intervals (Boaretto, 2022; Martin et al., 2020; Regev et al., 2014; Toffolo et al., 2014) are shown in Table 2. The age ranges we use for the archaeomagnetic analysis overlap the radiocarbon age ranges, but are not identical, as our age ranges incorporate additional archaeological information regarding the age range of the ceramic measured. Thus, the age range of a group may be as short as 50 years for sequences of short-lived phases punctuated by well-dated destruction layers (e.g., Q-4, Q-5, Q-6, and Q-7) or 250–300 years for less-constrained strata (e.g., J-4, J-5, and J-6).

3. The Levantine Archaeomagnetic Curve (LAC.v.1.0)

The Levantine Archaeomagnetic Curve (LAC) is designed to enable both the statistical analysis of secular variation properties and archaeomagnetic dating. In this article, we focus on the geomagnetic implications of the curve, whereas in a sister article (Vaknin et al., 2022), we demonstrate the applications of the curve

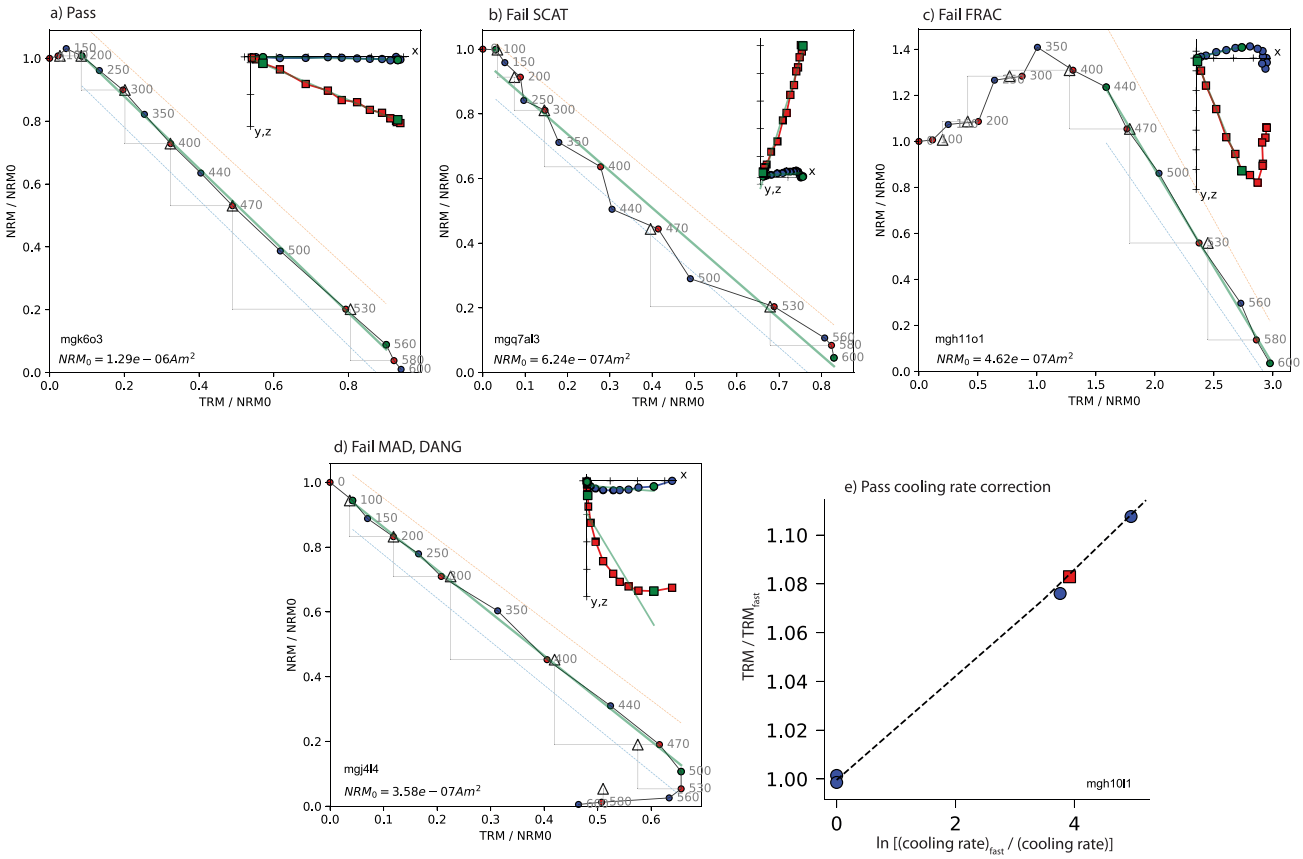

Figure 3. Representative results of specimen analysis conducted in this study. (a–d) Red circles, blue circles, and triangles in the main Arai plots are ZI steps, IZ steps, and pTRM checks, respectively. Heating temperatures (C°) are displayed near the symbols. Blue (red) squares in the inset Zijderveld plots are x–y (x–z) projections of the remaining natural remanent magnetization (NRM), where the x-axis is rotated to the direction of the NRM. The green line is the best fit. (a) Specimen passing all criteria. (b–d) Interpretations failing the SCAT (b), FRAC (c), and MAD + DANG (d) criteria. (e) A successful cooling rate experiment. Blue circles are four measurements at three different cooling rates, and the red square is a projection of the ancient cooling rate on the best-fit (dashed line).

for correlating ancient historical events. Preliminary versions of the LAC, using an identical methodology as in this study but spanning different time intervals, were published in Shaar et al. (2020) and Gallet et al. (2020). Here, we provide a short description of the different data sets used to construct the LAC and briefly outline the underlying methodology of the Bayesian analysis. A more detailed description of the archaeomagnetic methods, selection criteria, and our approach for sorting and organizing the published data can be found in Shaar et al. (2020). A complete description of the Bayesian method is given in Livermore et al. (2018).

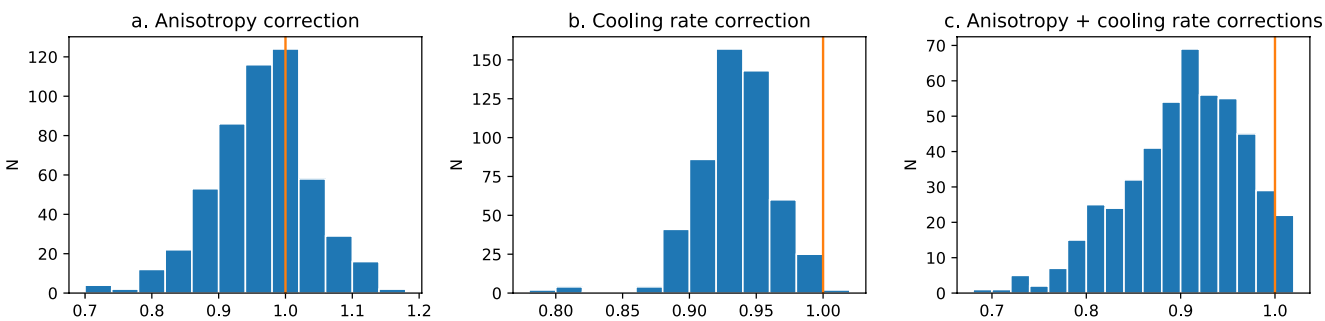

Figure 4. Histograms of anisotropy and cooling rate corrections.

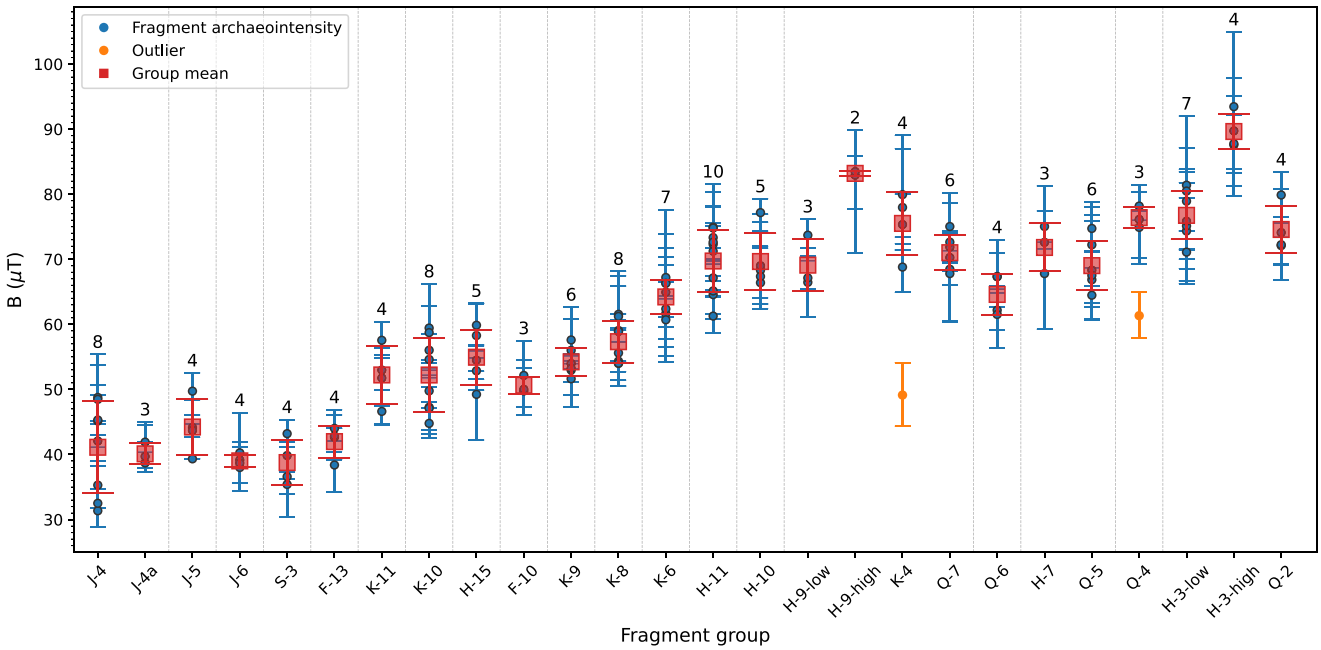

Figure 5. Archaeomagnetic stratigraphy of Tel Megiddo constructed from 132 samples. Full circles (red squares) represent the archaeointensity of samples (group means). Number of samples used to calculate the group means is indicated above each error bar. Vertical lines represent chrono-stratigraphic division. Fragment (sample) groups are plotted according to their relative age.

3.1. Data Compilation: Experimental Guidelines

Archaeomagnetic studies in the Levant and Mesopotamia, extending from Egypt in the south to southern Turkey in the north, have yielded an incredibly large archaeomagnetic data set, which includes more than 722 archaeointensity estimates published between 1969 and 2021. These are available in the GEOMAGIA50 database (Brown et al., 2015, 2021), the MagIC database (Tauxe et al., 2016), and the ArchaeoInt compilation (Genevey et al., 2008). Yet, when these data are simply stacked together, significant discrepancies are evident (Figure S1 in Supporting Information S1). From an experimental perspective, screening out the most robust data and using a consistent approach to uncertainty are not trivial tasks due to large differences in laboratory methods, data analysis approaches, and selection criteria. Moreover, not all of these data were published along with the raw measurement data, preventing a rigorous and identical calculation of the experimental uncertainty. We therefore adopt an approach that utilizes only methods that were tested against each other in different laboratories and shown to yield statistically indistinguishable results at the sample level:

- Thellier-IZZI-MagIC: This method incorporates the Thellier-IZZI protocol (Yu et al., 2004) exactly as applied in this study. The automatic interpretation procedure follows the STDEV-OPT algorithm (Shaar & Tauxe, 2013) with the "LAC criteria" provided in Table 1. All measurement data are available in the MagIC database (https://www.earthref.org/MagIC) and can be re-interpreted using any set of alternative selection criteria.
- Triaxe (Le Goff & Gallet, 2004) or the Triaxe + Coe (Gallet & Le Goff, 2006): The Triaxe method was tested against the Thellier-IZZI-MagIC in a blind test in Shaar et al. (2020) and yielded indistinguishable results. The Triaxe + Coe includes groups of specimens, which were analyzed using both the Thellier-Coe method (Coe et al., 1978) by Genevey et al. (2003) and the Triaxe method by Gallet and Le Goff (2006), and found to be equivalent.

Other data will be included in future LAC compilations if the measurement data can be analyzed using identical procedures and selection criteria as the rest of the LAC data.

Another aspect of the LAC compilation is associated with data hierarchy. A portion of the published archaeomagnetic data was reported as averages of specimens prepared from the same mother sample, while another portion was reported as averages of specimens or samples collected from the same archaeological context. In the

Table 2
Archaeointensity Results in Tel Megiddo

Megiddo group	Name in LAC.v.1.0[a]	Published radiocarbon age range 68.2% probability interval (95.4% probability interval) (BCE)[b]	Age range in LAC.v.1.0 compilation (BCE)[c]	*N* Samples	*n* Specimens	B (μT)	B σ (μT)	VADM (ZAm^2)	VADM σ (ZAm^2)
Q-2	mgq02	801–756 (805–735); Assyrian destruction level	820–732	4	15	74.6	3.6	140.3	6.9
H-3-low	mgh03-low	–	820–732	7	37	76.7	3.7	144.3	6.9
H-3-high	mgh03-high			4	18	89.6	2.7	168.6	5.1
Q-4	mgq04	897–821 (901–809)	890–840	3	14	76.4	1.7	143.7	3.1
Q-5	mgq05	956–894 (967–848)	925–875	6	30	69	3.8	129.8	7.1
H-7	Mgh07	930–900 (945–860)	925–875	3	16	71.8	3.7	135.1	6.9
Q-6	mgq06	979–911 (989–876)	950–900	4	16	64.6	3.2	121.5	6
Q-7	mgq07	1047–975 (1052–946)	1050–950	6	18	71	2.7	133.5	5.1
H-9-low	mgh09-low	1038–976 (1056–936)	1050–950	3	15	69.1	4	129.9	7.5
H-9-high	mgh09-high			2	9	83.2	0.4	156.5	0.7
K-4	mgk04	1037–951 (1053–908)	1050–950	4	15	75.5	4.9	142	9.1
H-10	mgh10	1068–1031 (1087–1023)	1100–1025	5	15	69.7	4.3	131	8.1
H-11	mgh11	1105–1051 (1115–1041)	1125–1075	10	30	69.7	4.8	131.1	9.1
K-6	mgk06	1148–1123 (1168–1104)	1175–1125	7	31	64.2	2.6	120.8	4.9
K-8	mgk08	1238–1178 (1268–1158)	1250–1175	8	33	57.3	3.2	107.8	6
K-9	mgk09	1323–1230 (1381–1201)	1400–1250	6	20	54.2	2.2	102	4.1
F-10	mgf10	1545–1354 (1561–1313)	1550–1400	3	14	50.6	1.3	95.2	2.5
H-15	mgh15	1557–1509 (1572–1463)	1550–1475	5	25	54.9	4.3	103.3	8
K–10	mgk10	1581–1545 (1596–1535)	1600–1550	8	35	52.2	5.7	98.2	10.7
K-11	mgk11	1626–1579 (1643–1561)	1650–1600	4	21	52.2	4.5	98.2	8.4
F–13	mgf13	–	1900–1700	4	25	42	2.5	78.9	4.6
S-3	mgs03	1942–1902 (1965–1886)	1950–1900	4	12	38.8	3.5	72.9	6.6
J-6	mgj06	2860–2540 (2880–2450)	2850–2500	4	15	39	0.9	73.4	1.8
J-5	mgj05	2920–2720 (2970–2670)	2900–2800	4	12	44.2	4.3	83.2	8
J-4[d]	mgj04	3060–2880 (3180–2830)	3100–2900	8	46	41.1	7.1	77.3	13.3
J-4a[d]	mgj04a	3060–2880 (3180–2830)	3100–2900	3	10	40.1	1.6	75.4	3.1

[a]Name in model data (Table S10). [b] Radiocarbon data from Regev et al. (2014), Toffolo et al. (2014), Martin et al. (2020), and Boaretto (2022). There are no radiocarbon data from H-03, and the age is linked to the Assyrian destruction level. Ages from S-3 are preliminary. There are no radiocarbon data from F-13, and the age is inferred from correlation to strata in areas *K* and *S*. [c] Age range used in the archaeomagnetic compilation and in Bayesian modeling. [d] J-4 and J-4a are two groups from the same level. J-4a fragments were collected from loci representing the final days of the temple, whereas the J-4 items originated from a fill context.

LAC compilation, we use the latter approach to avoid over (under)-representation of contexts with more (fewer) samples and to ensure that uncertainties are calculated consistently. Thus, each datum in the LAC compilation represents a "group," where a group can be, for example, a collection of indicative pottery from a specific stratum, fired mud bricks from a burnt structure, a layer in a slag mound, or storage jars with identical stamp types. The archaeointensity value of a group is calculated as an arithmetic mean of the samples' means after screening out outliers (e.g., K-4 and Q-4 in Figure 5). Two exceptions to this rule are related to destruction layers: a kiln from Horvat Tevet that had gone out of use when the site had been destroyed (Vaknin et al., 2022) and a clay-made floor burnt during the historically dated Babylonian destruction (Vaknin et al., 2020); in these cases, a large number of specimens collected from the same thermal unit are averaged.

Figure 6 displays 142 groups between 3000–500 BCE passing the experimental criteria. In order to minimize effects related to spatial variability of the field, we constrain the geographic distribution of the data to the region

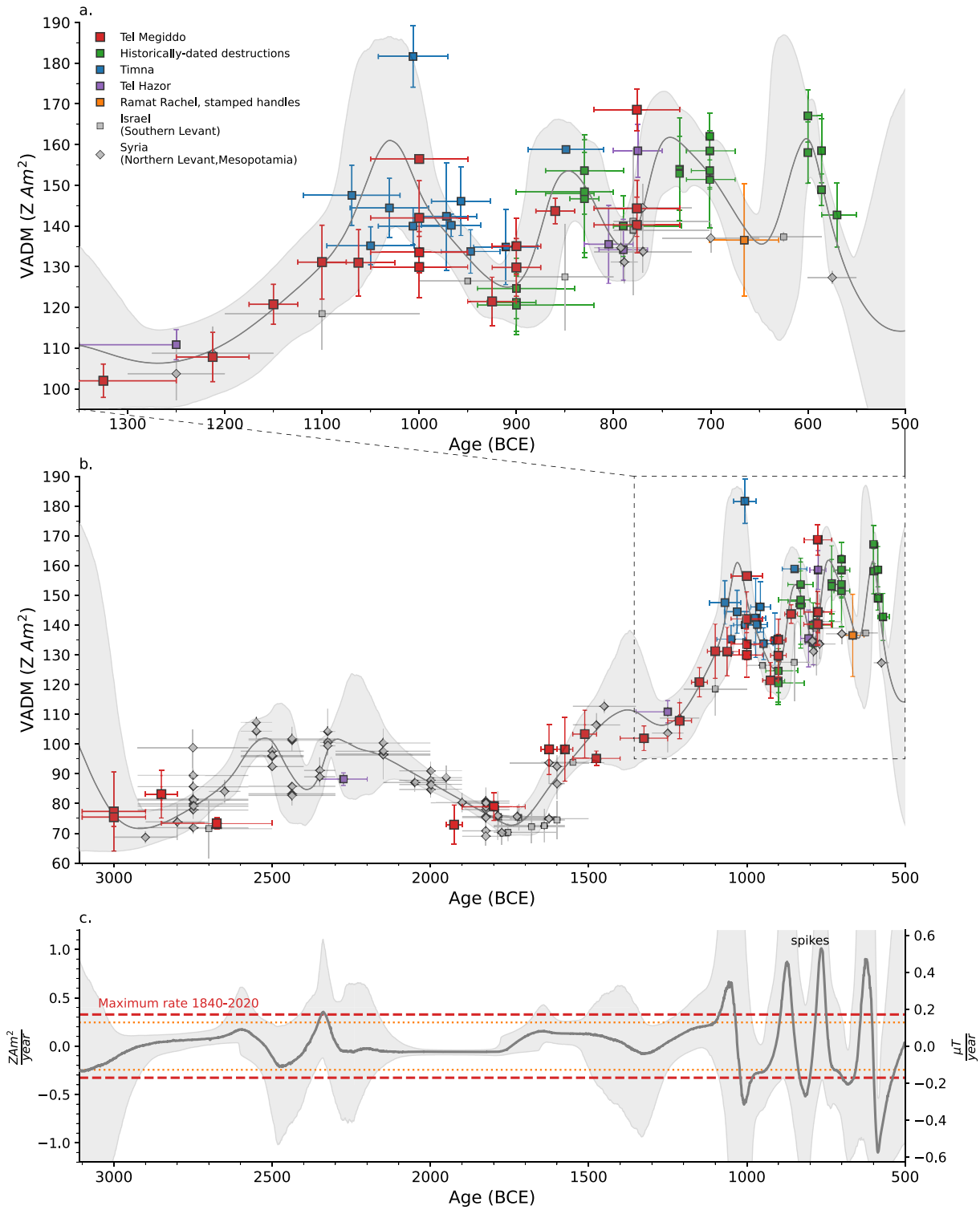

Figure 6. An archaeointensity curve. (a, b) Levantine Archaeomagnetic Intensity Curve (LAC.v.1.0). Colored symbols are groups of samples directly dated with radiocarbon or by clear association with dated historical events. Gray symbols represent groups dated using various archaeological methods. From the seventeenth to the sixth centuries, there is at least one directly dated context per century. Curve and shaded area in (a–b) are the average and the 95% credible interval calculated using the AH-RJMCMC algorithm (Livermore et al., 2018), respectively. (c) Rate of change. Dashed red and dotted orange lines show the maximum rate for 1840–2020 and the maximum rate in today's field (Figure 7), respectively. The oscillation pattern revealed in (a) includes four spikes with VADM > 150 ZAm^2 and a change rate of 0.35–0.55 μT/year (0.7–1.1 ZAm^2) (c).

that extends between southern Israel, Cyprus, northern Syria, and eastern Syria (Figure 1), comprising a circle with a radius of ∼500 km. Data are displayed in terms of virtual axial dipole moment (VADM)—a transformation from local, latitude-dependent field intensity measurement to the equivalent geomagnetic axial dipole moment. Data from Syria (analyzed using the Triaxe or Triaxe + Coe methods) representing Mesopotamia and northern Levant (Gallet & Al-Maqdissi, 2010; Gallet & Butterlin, 2015; Gallet et al., 2006, 2008, 2014, 2020; Genevey et al., 2003; Livermore et al., 2021), were reported as groups and displayed as published with a few minor updates on the ages of some fragment groups (Text S4 in Supporting Information S1 and the mentioned references for all the data obtained at the specimen/fragment levels). Data from Timna-30 slag mound (Shaar et al., 2011), Tel Hazor (Shaar et al., 2016), and the Judean stamped jars (Ben-Yosef et al., 2017), which were published as samples, are averaged to represent group means (Tables S4–S9 in Supporting Information S1).

3.2. Data Compilation: Age Estimation Guidelines

We distinguish between two sets of data with essentially different approaches for age estimation. The ages of the first set, marked in gray in Figure 6, were assigned by the excavators of the sites using a complex body of archaeological evidence that does not include absolute radiocarbon ages directly associated with the archaeointensity data. This raises two problems for paleomagnetists and modelers. First, tracing back the considerations used to determine the ages requires specific archaeological expertise, and, therefore, the quality, precision, and robustness of these ages cannot be easily assessed without a detailed description of the age data. Second, in many cases, the archaeological time scales, based on ceramic typology and cultural changes, might be loosely linked to an absolute age scale and may have different age interpretations. Our approach in these cases is to make as few changes as possible to the archaeological ages assigned by the excavators but rather to use wide age range that considers all possible correlations to the absolute age scale.

The ages of the color-coded data sets in Figure 6 are assigned using radiocarbon or direct associations to historical events whose ages are considered consensuses by most of the archaeological community. The latter are significant for the time interval associated with the Hallstatt Plateau (ca. 800–400 BCE) in the radiocarbon calibration curve (Reimer et al., 2020). From the eighth to sixth century BCE, the ages are based on a correlation with two precisely dated historical military campaigns described in the Hebrew Bible and other Mesopotamian texts—Assyrian (733–701 BCE) and Babylonian (600–586 BCE)—rather than on radiocarbon dating. In addition, the Aramean occupation (845–815 BCE), which is dated using both radiocarbon and historical constraints, is also used as a useful chronological anchor. The groups with age ranges tied to absolute ages are marked by four different colors in Figure 6, and include the following data sets:

- The radiocarbon-dated stratigraphy of Tel Megiddo described in this study, which ended in the Assyrian destruction of the city.
- Two radiocarbon-dated layers from Tel Hazor (Stratum XVIII, Stratum XII) and a sequence of three stratigraphically ordered, short-lived phases from strata V–VI that ended in the Assyrian destruction of Hazor (Text S1 and Tables S4–S5 in Supporting Information S1).
- A radiocarbon-dated sequence of 10 slag layers from Timna-30. The Bayesian age model of the mound (Shaar et al., 2011), which was originally established using a magnetostratigraphic correlation with Khirbet en-Nahas (Ben-Yosef et al., 2009), is revised here to include only radiocarbon samples collected from Timna-30 (Text S2 and Tables S6–S8 in Supporting Information S1)
- Materials dated by association to the Assyrian and Babylonian occupations or to the radiocarbon-dated Aramean campaign. This data set includes 19 burnt structures (Vaknin et al., 2020, 2022) and three groups of indicative ceramics that can be dated by association with cultural changes related to the occupations. The fired mud-brick structures found in the burnt level are crucial anchors for two reasons. First, as mentioned above, the uncertainty in radiocarbon dating in this period is in the order of 200–400 years due to the plateau in the calibration curve, while the dates of the historical campaigns are unique in their precision. Second, the burnt bricks record a single event, as the fire during the destruction resets their magnetization, in contrast to pottery groups that provide data over a time interval representing a production period.

Table S10 lists the VADM and the age range of 142 groups included in the LAC.v.1.0 compilation. We stress that none of the ages in the LAC data compilation were determined or constrained using archaeomagnetism in order to avoid circular reasoning.

3.3. Bayesian Modeling

With the data described in Section 3.2 and listed in Table S10, we calculate a Bayesian curve with its corresponding 95% confidence envelope (Figure 6 and Table S11). We term this curve "Levantine Archaeomagnetic Curve version 1.0", or LAC.v.1.0. The LAC is calculated using the age hyperparameter reverse-jump Monte Carlo Markov Chain (AH-RJMCMC) algorithm developed by Livermore et al. (2018) (https://github.com/plivermore/AH-RJMCMC1). The algorithm is based on a piece-wise linear interpolation of the data between vertices drawn in a random-walk-like perturbation within a space allowed by the acceptance criteria. The prior assumptions of the model are: (a) the allowed range of vertices' VADM values is set to between 60 and 200 ZAm^2; (b) the allowed number of vertices (K) is between $K_{min} = 1$ and $K_{max} = 150$; (c) ages in all contexts are uniformly distributed (equal probability of any age in the age range), except the data from Timna, which were modeled as normal distributions (Table S8 in Supporting Information S1); and (d) group means and standard deviations define a normal distribution of the archaeointensity data. In addition, Table S10 defines a stratigraphic order for contexts collected from the multi-layered sites (Tel Megiddo, Tel Hazor, Tell Atij, Tell Gudeda, Timna) and few mutual constraints between groups in Megiddo and Hazor. The AH-RJMCMC procedure takes into account all of these temporal relationships. The model uses the parameters $\sigma_{move} = 30$ years, $\sigma_{change} = 10$ ZAm^2, and $\sigma_{birth} = 10$ ZAm^2, which define the random perturbation of a vertex in age, in intensity, and that of the linearly interpolated intensity value of a new vertex based on the current vertex distribution respectively. The age of a single datum is perturbed per age-resampling step (num_age_changes = 1); the chain length is $2 \cdot 10^8$.

The sub-centennial resolution of the curve from 1100 to 550 BCE (encompassing the Levantine Iron Age anomaly) is achieved through several unique features of the combined data sets. First, we obtained radiocarbon-dated contexts with age uncertainties of approximately a century and, in several cases, even less. Second, the stratigraphic relationships in Timna, Megiddo, and Hazor define constraints to the Bayesian model that lead to a reduction in the posterior age ranges. Lastly, we included data obtained from historically well-dated burnt levels and used a dense data set with a large number of groups during the spike period.

4. Discussion

4.1. New Constraints on the Highest Geomagnetic Field Intensity

Considering all the published paleointensity estimates from individual samples (i.e., not group means) from the past 5 My available in the GEOMAGIA50 v.3.3 (Brown et al., 2015) and PINT v.8.1.0 (Biggin et al., 2009; Bono et al., 2022) databases, only 1% of the data, which are sporadically scattered in time and space, show VADM > 150 ZAm^2. As such, VADM values calculated from global geomagnetic models do not exceed 140 ZAm^2 (Arneitz et al., 2019; Constable et al., 2016; Korte & Constable, 2018; Panovska et al., 2019; Pavon-Carrasco et al., 2014). The only exception is the time interval between the end of the second millennium BCE and the middle of the first millennium BCE, where a number of archaeomagnetic observations point to high field values (>150 ZAm^2) at several locations: the Levant (Ben-Yosef et al., 2017; Ertepinar et al., 2012; Shaar et al., 2011, 2016; Vaknin et al., 2020), Caucasus (Shaar et al., 2017), China (Cai et al., 2017), Bulgaria (Kovacheva et al., 2014), Spain (Osete et al., 2020), Canary Islands (Kissel et al., 2015), Azores (Di Chiara et al., 2014) and Hawaii (Pressling et al., 2006). All these observations suggest short duration for the episodes of high intensity values. This behavior is probably associated with a more complex field structure than today's (Korte & Constable, 2018; Osete et al., 2020; Rivero-Montero et al., 2021) and, presumably, with a local high field anomaly in the Near East, termed the "Levantine Iron Age Anomaly" (LIAA) (Shaar et al., 2016, 2017, 2018).

The highest VADM values during the climax of the LIAA were termed "geomagnetic spikes" by Ben-Yosef et al. (2009) and Shaar et al. (2011). Note that we use the term "spike" hereafter in a dual sense: first, to describe a short time interval (about a century long) with rates of intensity change far exceeding those observed in the modern era (1840–2020), which would potentially allow for other spikes to be observed outside of the LIAA, and second, to describe short-lived intensity peaks exceeding the typical values in the geological record. Livermore et al. (2021) questioned the robustness of the spikes and stated that the number of spikes and their values strongly depend on the archaeomagnetic data used, particularly the experimental errors and the averaging scheme adopted (i.e., groups vs. individual samples). Here, we address the issues raised by Livermore et al. (2021) and assemble a much denser data set based solely on group averages. This way, each data point in our compilation represents exactly the same quantity and gains the same weight in the Bayesian calculation process. The new curve shows the

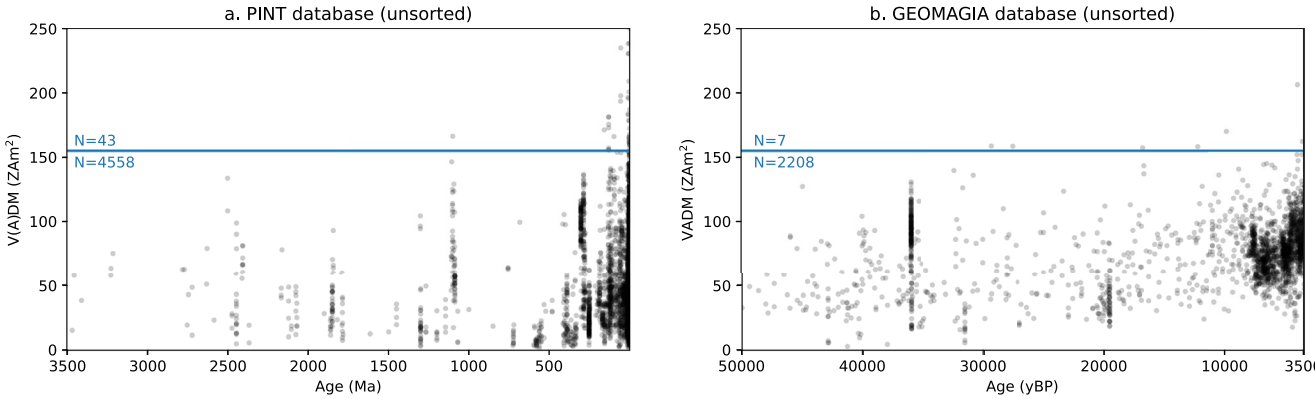

Figure 7. Comparison of spikes' paleointensity with the global databases. (a) PINT v.8.1.0 database (Bono et al., 2022). (b) GEOMAGIA50 v.3.3 (Brown et al., 2015) before 3500 yBP. Horizontal lines show the value of 155 ZAm^2 corresponding to the spike with the lowest intensity maximum according to LAC.v.1.0 (Figure 6). *N* is the number of paleointensity estimates below and above 155 ZAm^2.

occurrence of four spikes with peak VADM of 155–162 ZAm^2 around 1030, 840, 740, and 600 BCE. Each spike is represented by several coeval or nearly coeval groups, where overall, 14 groups have VADM > 150 ZAm^2. Considering that each group may represent a time average of several samples, we suggest a value of 155 ZAm^2 as a robust and conservative upper limit for the maximum field value. Yet, based on sample data, higher values may have occurred for short time intervals.

Spike-like intensity values appear rare in the paleomagnetic record, as shown in Figure 7 that displays all the published absolute paleointensity data with ages older than 1500 BCE from the GEOMAGIA50 and PINT databases. Only 49 data points out of 6,816 have field values higher than 155 ZAm^2, none of which pass the rather strict statistical tests applied in the LAC. Given the specific conditions associated with the Levantine geomagnetic spikes, the difficulty in detecting similar high-paleointensity values in the global paleointensity record is understandable. First, our dense data set, including 10 archaeointensity groups on average (each consisting of at least two samples) per century during the LIAA interval (Figure 6a) shows that the duration of the peaks is around a century. Thus, if an average of few samples is required to obtain a robust paleointensity estimate, a large data set, such as the LAC compilation, is required to detect spikes. Second, global geomagnetic models indicate that the geomagnetic dipole during the LIAA is most likely the highest in the Holocene (Constable et al., 2016; Pavon-Carrasco et al., 2014; Schanner et al., 2022). Thus, the likelihood of detecting spikes may depend on the likelihood that the ancient paleomagnetic dipole was similarly high. Third, the spikes are a regional feature associated with a local geomagnetic anomaly, expressed not only by high field values but also by directional deviations from a dipole field (Osete et al., 2020; Shaar et al., 2016, 2018). Consequently, there are low chances that the scattered and sparse paleointensity database spanning the geological record can reveal short-lived spikes. From the comparison with the global paleointensity database, we can conclude that based on the available data, spikes represent the highest value recorded so far and can serve as a robust upper boundary for the maximum strength of the geomagnetic field at a given location.

4.2. New Constraints to Maximum Secular Variation Rates

The rates associated with the spikes range between ~0.35–0.55 μT/year or 0.7–1.1 ZAm^2/year in VADM values (Figure 6c). To place these values within the context of the global geomagnetic field behavior, we calculate the maximum rate in today's field by observing the difference between the DGRF model epoch 2015 and the IGRF model epoch 2020 (Alken et al., 2021). For most of Earth's surface, the rates do not exceed 0.1 μT/year and a maximum rate of ~0.12 μT/year occurs only in limited areas shown in Figure 8a. VADM transformation accounting for the latitudinal dependency of the field yields a maximum rate of 0.25 ZAm^2/year (Figure 8b). We expand the calculation back to 1900 by looking at the maximum difference in field intensity every 5 years at any point on Earth's surface using IGRF (1900–1940) and DGRF (1950–2015) models (Alken et al., 2021). These models include high-precision satellite data from the past few decades as well as ground-based data that date back to the beginning of the twentieth century, where uncertainties in earlier models are greater compared to the satellite era (Beggan, 2022; Lowes, 2000). The DRGF models for the time interval 1940–1950 are not

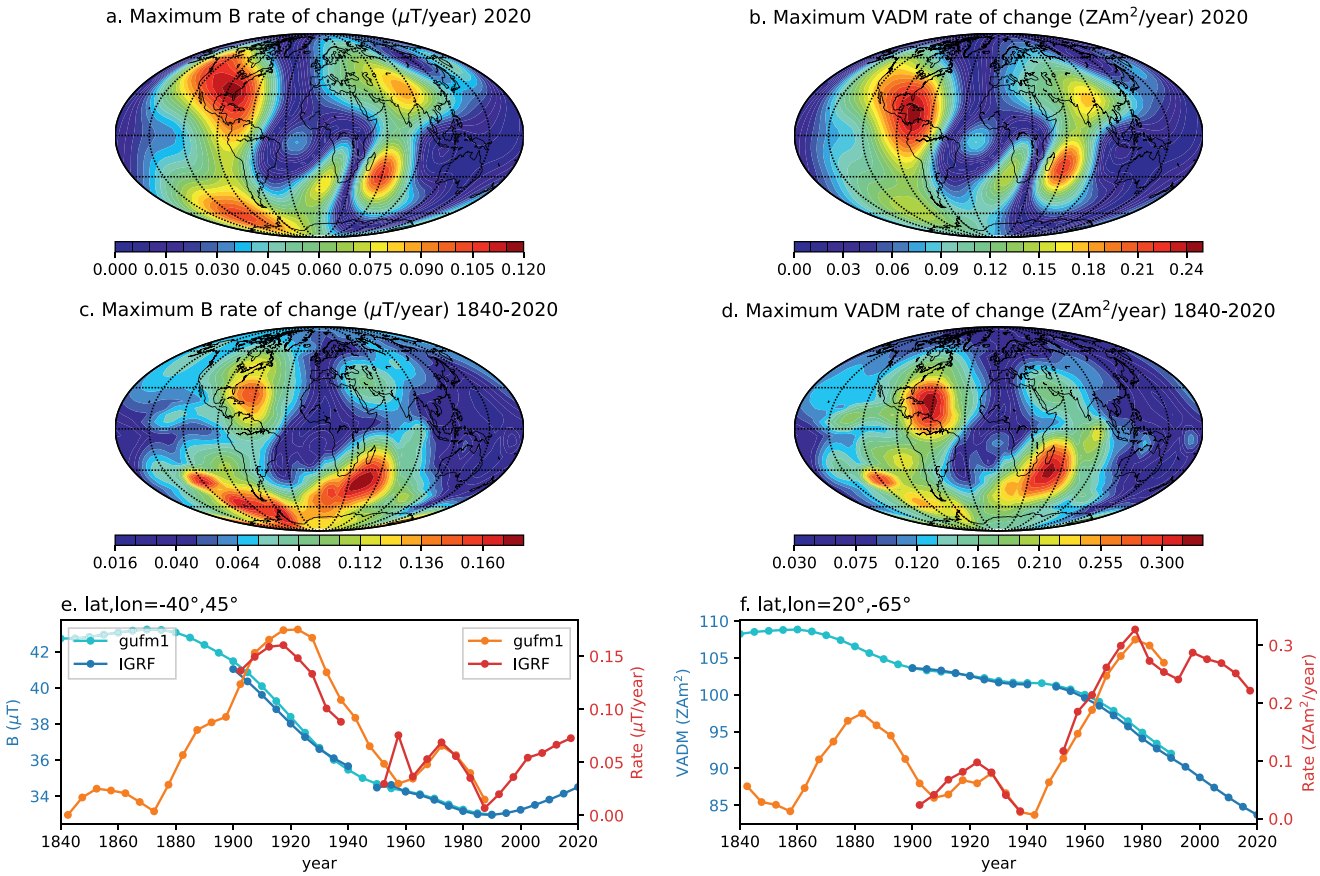

Figure 8. Maximum change rate of the geomagnetic field intensity for 1840–2020. (a–b) Intensity and VADM rate of change in today's field, calculated using the DGRF (2015) and IGRF (2020) models (Alken et al., 2021). (c–d) Maximum intensity and VADM rate of change for 1840–2020, calculated using the IGRF (1900–1940) and DGRF (1950–2015) models (Alken et al., 2021) and gufm1 (1840–1990) model (Jackson et al., 2000). (e) Field intensity and rate of change at the location with the maximum change in B. (f) virtual axial dipole moment (VADM) and rate of change at the location with the maximum change in VADM.

included because of unusual jumps in spherical harmonic coefficients with $n > 7$ (Xu, 2000) that cause abrupt changes in the rates at few locations, which are clearly an artifact. We repeat this calculation for 1840–1990 using the gufm1 model (Jackson et al., 2000), which was parametrized to form continuous representation of the field and therefore does not include the 1940–1950 jumps. Both DGRF/IGRF and gufm1 yield similar maximum rate of change in the past 180 years of 0.18 μT/year or 0.33 ZAm^2/year (Figures 8c–8f). These rates are apparently not significantly different today. Yet, they are considerably lower than those observed during the time intervals associated with geomagnetic spikes. Hence, LAC.v.1.0 also places new robust constraints on how fast local field intensity can change.

We note that the rates calculated using LAC.v.1.0 appear more moderate than previously considered (Ben-Yosef et al., 2009; Shaar et al., 2011), which had raised questions regarding the dynamo processes behind them (Livermore et al., 2014; Troyano et al., 2020). Although the spikes are now within the range of variations permitted by our current understanding of the geodynamo (Davies & Constable, 2017, 2018; Livermore et al., 2014), the fluctuations associated with the spikes remain unprecedented in their amplitude and rate.

4.3. Long-Term Evolution of the Levantine Iron Age Anomaly

The archaeo-magnetostratigraphy of Tel Megiddo reveals the Holocene's greatest amplitude change at multi-century scales between 1750 and 1030 BCE. The increase began with a minimum of 73 ZAm^2 in the eighteenth century BCE, a period characterized by the lowest intensities in the Near East over the last five millennia, comparable to the low values at the beginning of the third millennium BCE (Figure 6b). The 700 years-long increase is nearly continuous, punctuated by a century-scale peak around 1500 BCE. The spike period may,

therefore, be a climax of a long-term evolution in the geomagnetic field intensity in the Near East, which could result from the occurrence of intense and rapidly evolving flux bundles at the core-mantle boundary. It also contrasts with the period spanning from the third millennium BCE to the eighteenth century BCE, which shows intensity peaks of moderate amplitudes associated with lower change rates of less than 0.2 μT/year (Figures 6b and 6c; see also Gallet et al. (2020)). The significant increase in intensity would then result in spikes instead of intensity peaks, with the first events also being shorter and apparently more frequent, which could reflect a remarkable change in core dynamics.

5. Conclusions

We report the largest archaeomagnetic intensity data set currently available from a single site, that is, Tel Megiddo, with 23 sample groups collected from 18 consecutive radiocarbon-dated archaeological strata.

We assemble a new archaeomagnetic compilation of the Levant and Upper Mesopotamia between 3000 to 550 BCE with 142 different groups of samples. The interval from 1700 to 550 BCE is based mostly on contexts directly dated using radiocarbon and clear associations with well-dated historical military campaigns, providing an unprecedented sub-century resolution. We use this compilation to calculate the LAC (LAC.v.1.0), a Bayesian regional curve for high-precision archaeomagnetic dating.

The LAC depicts four geomagnetic spikes between 1050 and 600 BCE, each lasting about a century, defining new upper limits on both the maximum local field values and change rate. Considering the overall uncertainty, we suggest 155 ZAm^2 and 0.5 μT/year (1.0 ZAm^2/year in VADM values) as conservative upper boundaries for these quantities.

As a concluding remark, we highlight the challenge in constructing a robust, continuous geomagnetic intensity curve at a sub-centennial resolution over a large millennial time scales. This is made possible in this study by exploiting the advantage of the Near East's abundance of data that allows acquisition of large multiple archaeomagnetic data sets with precise dating, stratigraphic constraints, and cross-correlations between sites. In this respect, Tel Megiddo is an exemplary case study demonstrating a strong link between archaeology, radiocarbon, and geomagnetism.

Data Availability Statement

All measurement data are available in the MagIC database (https://earthref.org/MagIC/19395).

Acknowledgments
This project has received funding from the European Research Council (ERC) under the European Union's Horizon 2020 research and innovation programme (Grant agreement 804490) to RS. The study was partly supported by the Israel Science Foundation (ISF) Grant 1364/15 to RS. It was partly financed by the INSU-CNRS program PNP to YG. Work on the Megiddo samples was supported by the Dan David Foundation and grants from Mark Weissman and Jacques Chahine to IF. We thank Phil Livermore for assisting with the AH-RJMCMC analysis and Sanja Panovska for discussions that helped improve the manuscript. We thank Maxwell Brown and an anonymous reviewer for their careful reading and constructive comments.

References

Alken, P., Thebault, E., Beggan, C. D., Amit, H., Aubert, J., Baerenzung, J., et al. (2021). International geomagnetic reference field: The thirteenth generation. *Earth Planets and Space*, *73*(1), 49. https://doi.org/10.1186/s40623-020-01288-x

Arneitz, P., Egli, R., Leonhardt, R., & Fabian, K. (2019). A Bayesian iterative geomagnetic model with universal data input: Self-consistent spherical harmonic evolution for the geomagnetic field over the last 4000 years. *Physics of the Earth and Planetary Interiors*, *290*, 57–75. https://doi.org/10.1016/j.pepi.2019.03.008

Arneitz, P., Leonhardt, R., Schnepp, E., Heilig, B., Mayrhofer, F., Kovacs, P., et al. (2017). The HISTMAG database: Combining historical, archaeomagnetic and volcanic data. *Geophysical Journal International*, *210*(3), 1347–1359. https://doi.org/10.1093/gji/ggx245

Beggan, C. D. (2022). Evidence-based uncertainty estimates for the international geomagnetic reference field. *Earth Planets and Space*, *74*(1), 17. https://doi.org/10.1186/s40623-022-01572-y

Ben-Yosef, E., Millman, M., Shaar, R., Tauxe, L., & Lipschits, O. (2017). Six centuries of geomagnetic intensity variations recorded by royal Judean stamped jar handles. *Proceedings of the National Academy of Sciences of the United States of America*, *114*(9), 2160–2165. https://doi.org/10.1073/pnas.1615797114

Ben-Yosef, E., Tauxe, L., Levy, T. E., Shaar, R., Ron, H., & Najjar, M. (2009). Geomagnetic intensity spike recorded in high resolution slag deposit in Southern Jordan. *Earth and Planetary Science Letters*, *287*(3–4), 529–539. https://doi.org/10.1016/j.epsl.2009.09.001

Biggin, A. J., Strik, G. H. M. A., & Langereis, C. G. (2009). The intensity of the geomagnetic field in the late-Archaean: New measurements and an analysis of the updated IAGA palaeointensity database. *Earth Planets and Space*, *61*(1), 9–22. https://doi.org/10.1186/Bf03352881

Boaretto, E. (2022). Radiocarbon dating. In M. A. S. Martin & I. Finkelstein (Eds.), *Megiddo VI: The 2010–2014 Seasons*. State College.

Bono, R. K., Paterson, G. A., van der Boon, A., Engbers, Y. A., Grappone, J. M., Handford, B., et al. (2022). The PINT database: A definitive compilation of absolute palaeomagnetic intensity determinations since 4 billion years ago. *Geophysical Journal International*, *229*(1), 522–545. https://doi.org/10.1093/gji/ggab490

Brown, M. C., Donadini, F., Korte, M., Nilsson, A., Korhonen, K., Lodge, A., et al. (2015). GEOMAGIA50.v3: 1. General structure and modifications to the archeological and volcanic database. *Earth Planets and Space*, *67*, 1–31. https://doi.org/10.1186/s40623-015-0232-0

Brown, M. C., Herve, G., Korte, M., & Genevey, A. (2021). Global archaeomagnetic data: The state of the art and future challenges. *Physics of the Earth and Planetary Interiors*, *318*, 318. https://doi.org/10.1016/j.pepi.2021.106766

Cai, S. H., Jin, G. Y., Tauxe, L. S., Deng, C. L., Qin, H. F., Pan, Y. X., & Zhu, R. X. (2017). Archaeointensity results spanning the past 6 kiloyears from eastern China and implications for extreme behaviors of the geomagnetic field. *Proceedings of the National Academy of Sciences of the United States of America*, *114*(1), 39–44. https://doi.org/10.1073/pnas.1616976114

Campuzano, S. A., Gomez-Paccard, M., Pavon-Carrasco, F. J., & Osete, M. L. (2019). Emergence and evolution of the South Atlantic Anomaly revealed by the new paleomagnetic reconstruction SHAWQ2k. *Earth and Planetary Science Letters*, *512*, 17–26. https://doi.org/10.1016/j.epsl.2019.01.050

Coe, R., Gromme, S., & Mankinen, E. (1978). Geomagnetic paleointensities from radiocarbon-dated lava flows on Hawaii and question of Pacific nondipole low. *Journal of Geophysical Research*, *83*(B4), 1740–1756. https://doi.org/10.1029/JB083iB04p01740

Constable, C., Korte, M., & Panovska, S. (2016). Persistent high paleosecular variation activity in southern hemisphere for at least 10,000 years. *Earth and Planetary Science Letters*, *453*, 78–86. https://doi.org/10.1016/j.epsl.2016.08.015

Courtillot, V., & Le Mouel, J. L. (2007). The study of earth's magnetism (1269–1950): A foundation by peregrinus and subsequent development of geomagnetism and paleomagnetism. *Reviews of Geophysics*, *45*(3), RG3008. https://doi.org/10.1029/2006rg000198

Davies, C., & Constable, C. (2017). Geomagnetic spikes on the core-mantle boundary. *Nature Communications*, *8*(1), 15593. https://doi.org/10.1038/ncomms15593

Davies, C. J., & Constable, C. G. (2018). Searching for geomagnetic spikes in numerical dynamo simulations. *Earth and Planetary Science Letters*, *504*, 72–83. https://doi.org/10.1016/j.epsl.2018.09.037

Di Chiara, A., Tauxe, L., & Speranza, F. (2014). Paleointensity determination from Sao Miguel (Azores Archipelago) over the last 3 ka. *Physics of the Earth and Planetary Interiors*, *234*, 1–13. https://doi.org/10.1016/j.pepi.2014.06.008

Ertepinar, P., Langereis, C. G., Biggin, A. J., Frangipane, M., Matney, T., Okse, T., & Engin, A. (2012). Archaeomagnetic study of five mounds from Upper Mesopotamia between 2500 and 700 BCE: Further evidence for an extremely strong geomagnetic field ca. 3000 years ago. *Earth and Planetary Science Letters*, *357*, 84–98. https://doi.org/10.1016/j.epsl.2012.08.039

Finkelstein, I. (2009). Destructions: Megiddo as a case study. In J. D. Schloen (Ed.), *Exploring the Longue Durée* (pp. 113–126). Eisenbrauns.

Gallet, Y., & Al-Maqdissi, M. (2010). Archeomagnetism in Mishirfeh-Qatna: New data on the evolution of intensity in the earthly magnetic field in the Middle East during the last millenia. *Akkadica*, *131*(1), 29–46.

Gallet, Y., & Butterlin, P. (2015). Archaeological and geomagnetic implications of new archaeomagnetic intensity data from the early Bronze high Terrace "Massif Rouge' at Mari (Tell Hariri, Syria). *Archaeometry*, *57*, 263–276. https://doi.org/10.1111/arcm.12112

Gallet, Y., D'Andrea, M., Genevey, A., Pinnock, F., Le Goff, M., & Matthiae, P. (2014). Archaeomagnetism at Ebla (Tell Mardikh, Syria). New data on geomagnetic field intensity variations in the Near East during the Bronze age. *Journal of Archaeological Science*, *42*, 295–304. https://doi.org/10.1016/j.epsl.2017.11.013

Gallet, Y., Fortin, M., Fournier, A., Le Goff, M., & Livermore, P. (2020). Analysis of geomagnetic field intensity variations in Mesopotamia during the third millennium BC with archeological implications. *Earth and Planetary Science Letters*, *537*, 537. https://doi.org/10.1016/j.epsl.2020.116183

Gallet, Y., Genevey, A., Le Goff, M., Fluteau, F., & Ali Eshraghi, S. (2006). Possible impact of the Earth's magnetic field on the history of ancient civilizations. *Earth and Planetary Science Letters*, *246*(1–2), 17–26. https://doi.org/10.1016/j.epsl.2006.04.001

Gallet, Y., & Le Goff, M. (2006). High-temperature archeointensity measurements from Mesopotamia. *Earth and Planetary Science Letters*, *241*(1–2), 159–173. https://doi.org/10.1016/j.epsl.2005.09.058

Gallet, Y., Le Goff, M., Genevey, A., Margueron, J., & Matthiae, P. (2008). Geomagnetic field intensity behavior in the Middle East between similar to 3000 BC and similar to 1500 BC. *Geophysical Research Letters*, *35*(2), L02307. https://doi.org/10.1029/2007gl031991

Garcia, R., Perez-Rodriguez, N., Goguitchaichvili, A., Ceja, M. R., Morales, J., Soler, A. M., & Urrutia-Fucugauchi, J. (2021). On the absolute geomagnetic intensity fluctuations in Mexico over the last three millennia. *Journal of South American Earth Sciences*, *106*, 102927. https://doi.org/10.1016/j.jsames.2020.102927

Genevey, A., Gallet, Y., Constable, C. G., Korte, M., & Hulot, G. (2008). ArcheoInt: An upgraded compilation of geomagnetic field intensity data for the past ten millennia and its application to the recovery of the past dipole moment. *Geochemistry, Geophysics, Geosystems*, *9*(4), Q04038. https://doi.org/10.1029/2007gc001881

Genevey, A., Gallet, Y., Jesset, S., Thebault, E., Bouillon, J., Lefevre, A., & Le Goff, M. (2016). New archeointensity data from French Early Medieval pottery production (6th–10th century AD). Tracing 1500 years of geomagnetic field intensity variations in Western Europe. *Physics of the Earth and Planetary Interiors*, *257*, 205–219. https://doi.org/10.1016/j.pepi.2016.06.001

Genevey, A., Gallet, Y., Thebault, E., Livermore, P. W., Fournier, A., Jesset, S., et al. (2021). Archeomagnetic intensity investigations of French medieval ceramic workshops: Contribution to regional field modeling and archeointensity-based dating. *Physics of the Earth and Planetary Interiors*, *318*, 318. https://doi.org/10.1016/j.pepi.2021.106750

Genevey, A. S., Gallet, Y., & Margueron, J. C. (2003). Eight thousand years of geomagnetic field intensity variations in the eastern Mediterranean. *Journal of Geophysical Research*, *108*(B5). https://doi.org/10.1029/2001jb001612

Jackson, A., Jonkers, A. R. T., & Walker, M. R. (2000). Four centuries of geomagnetic secular variation from historical records. *Philosophical Transactions of the Royal Society of London Series A-Mathematical Physical and Engineering Sciences*, *358*(1768), 957–990. https://doi.org/10.1098/rsta.2000.0569

Kirschvink, J. L. (1980). The least-squares line and plane and the analysis of paleomagnetic data. *Geophysical Journal of the Royal Astronomical Society*, *62*(3), 699–718. https://doi.org/10.1111/j.1365-246X.1980.tb02601.x

Kissel, C., Laj, C., Rodriguez-Gonzalez, A., Perez-Torrado, F., Carracedo, J. C., & Wandres, C. (2015). Holocene geomagnetic field intensity variations: Contribution from the low latitude Canary Islands site. *Earth and Planetary Science Letters*, *430*, 178–190. https://doi.org/10.1016/j.epsl.2015.08.005

Korte, M., & Constable, C. G. (2018). Archeomagnetic intensity spikes: Global or regional geomagnetic field features? *Frontiers of Earth Science*, *6*, 1–15. https://doi.org/10.3389/feart.2018.00017

Kovacheva, M., Kostadinova-Avramova, M., Jordanova, N., Lanos, P., & Boyadzhiev, Y. (2014). Extended and revised archaeomagnetic database and secular variation curves from Bulgaria for the last eight millennia. *Physics of the Earth and Planetary Interiors*, *236*, 79–94. https://doi.org/10.1016/j.pepi.2014.07.002

Le Goff, M., & Gallet, Y. (2004). A new three-axis vibrating sample magnetometer for continuous high-temperature magnetization measurements: Applications to paleo- and archeo-intensity determinations. *Earth and Planetary Science Letters*, *229*(1–2), 31–43. https://doi.org/10.1016/j.epsl.2004.10.025

Livermore, P. W., Fournier, A., & Gallet, Y. (2014). Core-flow constraints on extreme archeomagnetic intensity changes. *Earth and Planetary Science Letters*, *387*, 145–156. https://doi.org/10.1016/j.epsl.2013.11.020

Livermore, P. W., Fournier, A., Gallet, Y., & Bodin, T. (2018). Transdimensional inference of archeomagnetic intensity change. *Geophysical Journal International*, *215*(3), 2008–2034. https://doi.org/10.1093/gji/ggy383

Livermore, P. W., Gallet, Y., & Fournier, A. (2021). Archeomagnetic intensity variations during the era of geomagnetic spikes in the Levant. *Physics of the Earth and Planetary Interiors*, *312*, 312. https://doi.org/10.1016/j.pepi.2021.106657

Lowes, F. J. (2000). An estimate of the errors of the IGRF-DGRF fields 1945-2000. *Earth Planets and Space*, *52*(12), 1207–1211. https://doi.org/10.1186/Bf03352353

Martin, M. A. S., Finkelstein, I., & Piasetzky, E. (2020). Radiocarbon-dating the late Bronze age: Cultural and historical considerations on Megiddo and beyond. *Bulletin of the American Schools of Oriental Research*, *384*, 211–240. https://doi.org/10.1086/709576

Nilsson, A., Holme, R., Korte, M., Suttie, N., & Hill, M. (2014). Reconstructing Holocene geomagnetic field variation: New methods, models and implications. *Geophysical Journal International*, *198*(1), 229–248. https://doi.org/10.1093/gji/ggu120

Nilsson, A., Suttie, N., Stoner, J. S., & Muscheler, R. (2022). Recurrent ancient geomagnetic field anomalies shed light on future evolution of the South Atlantic Anomaly. *Proceedings of the National Academy of Sciences*, *119*(24), e2200749119. https://doi.org/10.1073/pnas.2200749119

Osete, M. L., Molina-Cardin, A., Campuzano, S. A., Aguilella-Arzo, G., Barrachina-Ibanez, A., Falomir-Granell, F., et al. (2020). Two archaeomagnetic intensity maxima and rapid directional variation rates during the Early Iron Age observed at Iberian coordinates. Implications on the evolution of the Levantine Iron Age Anomaly. *Earth and Planetary Science Letters*, *533*, 533. https://doi.org/10.1016/j.epsl.2019.116047

Panovska, S., Korte, M., & Constable, C. G. (2019). One hundred thousand years of geomagnetic field evolution. *Reviews of Geophysics*, *57*(4), 1289–1337. https://doi.org/10.1029/2019rg000656

Paterson, G. A., Tauxe, L., Biggin, A. J., Shaar, R., & Jonestrask, L. C. (2014). On improving the selection of Thellier-type paleointensity data. *Geochemistry, Geophysics, Geosystems*, *15*(4), 1180–1192. https://doi.org/10.1002/2013gc005135

Pavon-Carrasco, F. J., Osete, M. L., Torta, J. M., & De Santis, A. (2014). A geomagnetic field model for the Holocene based on archaeomagnetic and lava flow data. *Earth and Planetary Science Letters*, *388*, 98–109. https://doi.org/10.1016/j.epsl.2013.11.046

Pressling, N., Laj, C., Kissel, C., Champion, D., & Gubbins, D. (2006). Palaeomagnetic intensities from C-14-dated lava flows on the big Island, Hawaii: 0–21 kyr. *Earth and Planetary Science Letters*, *247*(1–2), 26–40. https://doi.org/10.1016/j.epsl.2006.04.026

Regev, J., Finkelstein, I., Adams, M. J., & Elisabetta, B. (2014). Wiggled-matched ^{14}C chronology of early Bronze Megiddo and the synchronization of Egyptian and Levantine chronologies. *Egypt and the Levant*, *24*, 241–264. https://doi.org/10.1553/s241

Reimer, P. J., Austin, W. E. N., Bard, E., Bayliss, A., Blackwell, P. G., Ramsey, C. B., et al. (2020). The Intcal20 Northern hemisphere radiocarbon age calibration curve (0–55 Cal Kbp). *Radiocarbon*, *62*(4), 725–757. https://doi.org/10.1017/Rdc.2020.41

Rivero-Montero, M., Gomez-Paccard, M., Pavon-Carrasco, F. J., Cau-Ontiveros, M. A., Fantuzzi, L., Martin-Hernandez, F., et al. (2021). Refining geomagnetic field intensity changes in Europe between 200 CE and 1800 CE. New data from the Mediterranean region. *Physics of the Earth and Planetary Interiors*, *317*, 317. https://doi.org/10.1016/j.pepi.2021.106749

Schanner, M., Korte, M., & Holschneider, M. (2022). ArchKalmag14k: A Kalman-filter based global geomagnetic model for the Holocene. *Journal of Geophysical Research: Solid Earth*, *127*(2). https://doi.org/10.1029/2021JB023166

Schnepp, E., Thallner, D., Arneitz, P., & Leonhardt, R. (2020). New archeomagnetic secular variation data from Central Europe, II: Intensities. *Physics of the Earth and Planetary Interiors*, *309*, 106605. https://doi.org/10.1016/j.pepi.2020.106605

Selkin, P. A., & Tauxe, L. (2000). Long-term variations in palaeointensity. *Philosophical Transactions of the Royal Society A: Mathematical, Physical & Engineering Sciences*, *358*(1768), 1065–1088.

Shaar, R., Bechar, S., Finkelstein, I., Gallet, Y., Martin, M. A. S., Ebert, Y., et al. (2020). Synchronizing geomagnetic field intensity records in the Levant between the 23rd and 15th centuries BCE: Chronological and methodological implications. *Geochemistry, Geophysics, Geosystems*, *21*(12). https://doi.org/10.1029/2020GC009251

Shaar, R., Ben-Yosef, E., Ron, H., Tauxe, L., Agnon, A., & Kessel, R. (2011). Geomagnetic field intensity: How high can it get? How fast can it change? Constraints from Iron Age copper slag. *Earth and Planetary Science Letters*, *301*(1–2), 297–306. https://doi.org/10.1016/j.epsl.2010.11.013

Shaar, R., Hassul, E., Raphael, K., Ebert, Y., Segal, Y., Eden, I., et al. (2018). The first catalog of archaeomagnetic directions from Israel with 4,000 years of geomagnetic secular variations. *Frontiers of Earth Science*, *6*. https://doi.org/10.3389/feart.2018.00164

Shaar, R., & Tauxe, L. (2013). Thellier GUI: An integrated tool for analyzing paleointensity data from Thellier-type experiments. *Geochemistry, Geophysics, Geosystems*, *14*(3), 677–692. https://doi.org/10.1002/ggge.20062

Shaar, R., Tauxe, L., Ben-Yosef, E., Kassianidou, V., Lorentzen, B., Feinberg, J. M., & Levy, T. E. (2015). Decadal-scale variations in geomagnetic field intensity from ancient Cypriot slag mounds. *Geochemistry, Geophysics, Geosystems*, *16*(1), 195–214. https://doi.org/10.1002/2014gc005455

Shaar, R., Tauxe, L., Goguitchaichvili, A., Devidze, M., & Licheli, V. (2017). Further evidence of the Levantine Iron Age geomagnetic anomaly from Georgian pottery. *Geophysical Research Letters*, *44*(5), 2229–2236. https://doi.org/10.1002/2016gl071494

Shaar, R., Tauxe, L., Ron, H., Ebert, Y., Zuckerman, S., Finkelstein, I., & Agnon, A. (2016). Large geomagnetic field anomalies revealed in Bronze to Iron Age archeomagnetic data from Tel Megiddo and Tel Hazor, Israel. *Earth and Planetary Science Letters*, *442*, 173–185. https://doi.org/10.1016/j.epsl.2016.02.038

Tauxe, L., Shaar, R., Jonestrask, L., Swanson-Hysell, N. L., Minnett, R., Koppers, A. A. P., et al. (2016). PmagPy: Software package for paleomagnetic data analysis and a bridge to the magnetics information Consortium (MagIC) database. *Geochemistry, Geophysics, Geosystems*, *17*(6), 2450–2463. https://doi.org/10.1002/2016gc006307

Tauxe, L., & Staudigel, H. (2004). Strength of the geomagnetic field in the Cretaceous normal Superchron: New data from submarine basaltic glass of the Troodos Ophiolite. *Geochemistry, Geophysics, Geosystems*, *5*(2), Q02H06. https://doi.org/10.1029/2003GC000635

Toffolo, M. B., Arie, E., Martin, M. A. S., Boaretto, E., & Finkelstein, I. (2014). Absolute chronology of Megiddo, Israel, in the late Bronze and Iron Ages: High-resolution radiocarbon dating. *Radiocarbon*, *56*(1), 221–244. https://doi.org/10.2458/56.16899

Troyano, M., Fournier, A., Gallet, Y., & Finlay, C. C. (2020). Imprint of magnetic flux expulsion at the core-mantle boundary on geomagnetic field intensity variations. *Geophysical Journal International*, *221*(3), 1984–2009. https://doi.org/10.1093/gji/ggaa126

Vaknin, Y., Shaar, R., Gadot, Y., Shalev, Y., Lipschits, O., & Ben-Yosef, E. (2020). The Earth's magnetic field in Jerusalem during the Babylonian destruction: A unique reference for field behavior and an anchor for archaeomagnetic dating. *PLoS One*, *15*(8), e0237029. https://doi.org/10.1371/journal.pone.0237029

Vaknin, Y., Shaar, R., Lipschits, O., Mazar, A., Maeir, A., Garfinkel, Y., et al. (2022). Reconstructing biblical military campaigns using geomagnetic field data. *Proceedings of the National Academy of Sciences*, *119*(44). https://doi.org/10.1073/pnas.2209117119

Xu, W. Y. (2000). Unusual behaviour of the IGRF during the 1945–1955 period. *Earth Planets and Space*, *52*(12), 1227–1233. https://doi.org/10.1186/Bf03352355

Yu, Y. J., Tauxe, L., & Genevey, A. (2004). Toward an optimal geomagnetic field intensity determination technique. *Geochemistry, Geophysics, Geosystems*, *5*(2). https://doi.org/10.1029/2003gc000630